

# Cosmic rays and the magnetic field in the nearby starburst galaxy NGC 253

## I. The distribution and transport of cosmic rays

V. Heesen<sup>1</sup>, R. Beck<sup>2</sup>, M. Krause<sup>2</sup>, and R.-J. Dettmar<sup>1</sup>

<sup>1</sup> Astronomisches Institut der Ruhr-Universität Bochum, Universitätsstr. 150, 44780 Bochum, Germany  
e-mail: heesen@astro.rub.de

<sup>2</sup> Max-Planck Institut für Radioastronomie, Auf dem Hügel 69, 53121 Bonn, Germany

Received 8 July 2008 / Accepted 28 November 2008

### ABSTRACT

**Context.** Nearby edge-on galaxies showing a synchrotron halo are nearly ideal objects for studying the transport of cosmic rays (CRs) in galaxies. Among them, the nearby starburst galaxy NGC 253 hosts a galactic wind indicated by various ISM phases in its halo.

**Aims.** The diffusive and convective CR transport from the disk into the halo is investigated using the local CR bulk speed. The connection between the CR transport and the galactic wind is outlined.

**Methods.** We observed NGC 253 with the VLA at  $\lambda 6.2$  cm in a mosaic with 15 pointings. The missing zero-spacing flux density of the VLA mosaic was filled in using observations with the 100-m Effelsberg telescope. We also obtained a new  $\lambda 3.6$  cm map from Effelsberg observations and reproduced VLA maps at  $\lambda 20$  cm and  $\lambda 90$  cm. The high dynamic range needed due to the strong nuclear point-like source was addressed with a special data calibration scheme for both the single-dish and the interferometric observations.

**Results.** We find a thin and a thick radio disk with exponential scaleheights of 0.3 kpc and 1.7 kpc at  $\lambda 6.2$  cm. The equipartition total magnetic field strength between  $7 \mu\text{G}$  and  $18 \mu\text{G}$  in the disk is remarkably high. We use the spectral aging of the cosmic ray electrons (CREs) seen in the vertical profiles of the spectral index to determine a lower limit for the global CR bulk speed as  $170 \pm 70 \text{ km s}^{-1}$ . The linear correlation between the scaleheights and the CRE lifetimes, as evident from the dumbbell shaped halo, requires a vertical CR transport with a bulk speed of  $300 \pm 30 \text{ km s}^{-1}$  in the northeastern halo, similar to the escape velocity of  $280 \text{ km s}^{-1}$ . This shows the presence of a “disk wind” in NGC 253. In the southwestern halo, the transport is mainly diffusive with a diffusion coefficient of  $2.0 \pm 0.2 \times 10^{29} \text{ cm}^2 \text{ s}^{-1}$ .

**Conclusions.** Measuring the radio synchrotron scaleheight and estimating the CRE lifetime allow us to determine the bulk speed of the CR transport into the halo. The transport is convective and more efficient in the northeastern halo, while it is diffusive in the southwestern halo. The luminous material is transported by the disk wind, which can explain the different amounts of extra-planar H I, H $\alpha$ , and soft X-ray emission in the two halo parts. Future low-frequency radio observations will provide the data to analyze the vertical velocity profile of galactic winds.

**Key words.** galaxies: individual: NGC 253 – ISM: cosmic rays – methods: observational – methods: data analysis – galaxies: halos – galaxies: ISM

## 1. Introduction

NGC 253 is a prototypical starburst galaxy at a distance of 3.94 Mpc (Karachentsev et al. 2003). It is a late-type spiral galaxy with a high inclination angle of  $78.5^\circ \pm 0.5^\circ$  (Pence 1980). This allows observations of extra-planar components of the interstellar medium (ISM) at different wavelengths: ROSAT Position Sensitive Proportional Counter (PSPC) observations have revealed a very extended halo of soft diffuse X-ray emission extending into the halo to a distance of 8 kpc from the disk. The prominent lobes of soft X-ray emission show a distinct “X”-shaped pattern centered on the nucleus (Pietsch et al. 2000). Moreover, H $\alpha$  observations by Hoopes et al. (1996) show plumes emerging from the disk into the halo, which spatially coincide with the lobes of the soft X-ray emission. Observations of Boomsma et al. (2005) in H I show large plumes of extra-planar H I emission enclosing the soft X-ray emission.

Given the different phases of the ISM in the halo of NGC 253, the question arises of how the observed halo structure was formed. The distribution of the different ISM phases in

shells has led to the suggestion that the halo can be considered as one huge bubble that is fueled by an active star-forming region around the nucleus of the galaxy (Strickland et al. 2002). This scenario is supported by the finding of a small plume of hot X-ray gas in CHANDRA maps associated with a conical outflow from the nuclear starburst (Strickland et al. 2000). Spectroscopic measurements of H $\alpha$ -emitting gas in the southern nuclear outflow cone by Schulz & Wegner (1992) give an outflow velocity of  $390 \text{ km s}^{-1}$ . Numerical models by Suchkov et al. (1994) follow the evolution of a multi-phase halo powered by a compact source located in the center of the disk. A close resemblance of the “X”-shaped pattern of the soft X-ray emission was indeed found, which could be interpreted as the termination shock of the hot gas where the gas cools effectively.

A possible explanation for the amount of X-ray and H $\alpha$ -emitting gas in the halo is the dissipation of kinetic energy via shock heating (Lehnert & Heckman 1996) if the thermalization fraction is high enough (Strickland et al. 2002). A precondition for this model is the existence of cool gas in the halo that condenses to clouds from which the shock can form.

ISOPHOT observations discussed by Radovich et al. (2001) show “X”-shaped far-infrared emission overlapping with the H $\alpha$  and X-ray emission, indicating the existence of such a cool gas. However, the origin of the gas is not clear. It could be a pre-existing population of cool gas in the halo, possibly accreted from a merger with a satellite. Another possibility is that the gas of the disk can be transported into the halo along the walls of the cavity as Kelvin-Helmholtz instabilities rip off clumps of cool gas in the disk (see e.g. Suchkov et al. 1994; Heckman et al. 2000). Summarizing, it is important to understand how the gas is transported from the disk into the halo.

Cosmic rays (CRs) and magnetic fields are important for the evolution of the ISM, because they may possess an energy density comparable to that of the thermal gas (Beck et al. 1996). They are even more important for the study of galactic winds, because the thermal gas itself can drive a galactic wind only when the heating processes are sufficiently strong and the gravitational potential is comparably weak. A good example of this situation is the edge-on galaxy M 82, which possesses a huge halo of hot X-ray, H $\alpha$ , and radio continuum emission. However, the hot gas cools radiatively preventing the escape from the gravitational potential and falls back onto the disk in condensed clouds. This *galactic fountain* scenario proposed by Field et al. (1969) might explain the infall of the so-called High Velocity Clouds that could be interpreted as cooled remnants of the hot gas.

If we incorporate the CR pressure the galactic wind can be sustained against the radiative losses (Ipavich 1975), because the CRs suffer only little from radiative losses (mainly via synchrotron losses of the electrons). As the protons carry most of the energy this does not influence the CR energy density. Thus the pressure support from below can drive a galactic wind against the gravity of the underlying galactic disk. Breitschwerdt et al. (1991, 1993) started a series of papers treating the CR transport along “flux density tubes” in a one-dimensional model. This model was extended to a full three-dimensional treatment (with rotational symmetry) by Zirakashvili et al. (1996), including the influence of galactic rotation. It was found that CRs can drive a galactic wind under a broad variety of conditions in the disk and that the loss of mass and momentum over the lifetime of a galaxy is significant (Ptuskin et al. 1997). A recent study by Everett et al. (2008) showed that the extra-planar X-ray emission in the Milky Way can be explained by a CR driven galactic wind.

The theory of a CR driven galactic wind can be constrained with radio continuum studies: as the relativistic CRs are the most pervasive component of the ISM, they are expected to be associated with the other phases in the halo of NGC 253. Indeed, a radio halo around NGC 253 was detected by Beck et al. (1979) using the 100-m Effelsberg telescope at  $\lambda$ 3.6 cm. However, no correction for the sidelobes of the strong nuclear point-like source was applied and thus it was not possible to disentangle the intrinsic halo emission from the contribution by the sidelobes. The study was extended later with VLA interferometric observations by Carilli et al. (1992), which show an extended radio halo over the length of the optical disk very different in shape from the halo seen in X-rays. The finding of a large “radio spur” southeast of the nucleus already led to speculations of an outflow connected with the spur.

Extending the observations to other wavelengths and including polarization, a prediction of the magnetic field structure in the disk was presented by Beck et al. (1994). The sensitivity of the observations, however, was not sufficient to get information for the extra-planar polarized emission so that the magnetic field structure in the halo could not be determined. With the new

VLA mosaic at  $\lambda$ 6.2 cm we are able to increase the sensitivity at short wavelengths, allowing us to study in detail the extra-planar emission and possible relations to the outflow of hot gas. The advantage is that the high synchrotron losses at this short wavelength impose tighter constraints on the CR transport from the disk into the halo. Moreover, for the first time sensitive polarization measurements were carried out to study the large-scale magnetic field structure in the halo of NGC 253, which will be addressed in a subsequent paper (thereafter Paper II).

This paper is organized as follows: in Sect. 2 we introduce our observations and present the data reduction. We present our radio continuum maps along with a discussion of the morphology in Sect. 3. The distribution of the radio spectral index is presented in Sect. 4. The finding of an extended radio halo with a thick radio disk leads to the determination of the vertical CR bulk speed (Sect. 5). In Sect. 6 we discuss the impact of our findings on the feeding of the radio halo with CRs from the star-forming disk. Finally, we summarize our results and present our conclusions in Sect. 7.

## 2. Observations and data reduction

### 2.1. The Effelsberg observations

For the single-dish observations at  $\lambda$ 3.6 cm and  $\lambda$ 6.2 cm of NGC 253 we used the Effelsberg 100-m telescope<sup>1</sup>. The  $\lambda$ 3.6 cm observations were obtained between February 2003 and July 2004 with a single-horn receiver mounted in the secondary focus cabin (SFK). We used the broad band receiver channel centered at 8.35 GHz which has a bandwidth of 1.1 GHz. The  $\lambda$ 6.2 cm observations were carried out in 1997 with a dual-horn receiver mounted in the SFK using a bandwidth of 500 MHz centered at 4.85 GHz. Both receivers are capable to record the total intensity and the Stokes channels  $Q$  and  $U$  simultaneously. As primary (flux) calibrator we used 3C 286 adopting the flux density scale of Baars et al. (1977).

We observed 26 maps at  $\lambda$ 3.6 cm with a map size of  $30' \times 20'$ . Two perpendicular scanning directions were aligned with the major/minor axis of NGC 253 (PA =  $52^\circ$ ), in order to reduce the time for scanning. For the  $\lambda$ 6.2 cm observations we made use of the “software beam switching” technique described in Morsi & Reich (1986). Since the observations with the dual-horn are made in the azimuth-elevation coordinate system, we used a restoration method (see Emerson et al. 1979) to obtain eleven maps with a size of  $30' \times 30'$ .

The data reduction was performed using NOD2 data reduction package (Haslam 1974). Each map was checked and corrected for pointing errors using Gaussian fits on the nuclear point-like source in NGC 253. The final map was produced using the PLAIT algorithm, which we used to suppress scanning effects (Emerson & Gräve 1988). The noise level of the final map at  $\lambda$ 3.6 cm is  $500 \mu\text{Jy}/\text{beam}$  in total power with a resolution of  $84''^2$ . At  $\lambda$ 6.2 cm a noise level of  $1 \text{ mJy}/\text{beam}$  with a resolution of  $144''$  was achieved.

The sidelobes of the Effelsberg beam pattern peak at a level of a few % which limits the dynamic range to 100 at most. As the nuclear point-like source has a flux density of  $1 \text{ Jy}$ , we would be limited to a noise level of  $10 \text{ mJy}/\text{beam}$ . In order to overcome these limitations we had to remove the sidelobes of the nuclear

<sup>1</sup> The Effelsberg 100-m telescope is operated by the Max-Planck Institut für Radioastronomie (MPIfR).

<sup>2</sup> All angular resolutions in this paper are referred to as the Half Power Beam Width (HPBW).

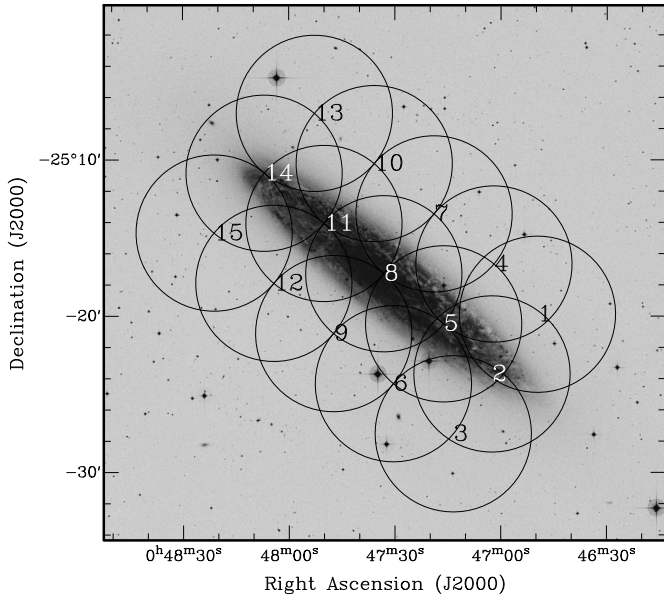


**Fig. 1.** The VLA mosaic of NGC 253 at  $\lambda 6.2$  cm consisting of 15 pointings. The circles indicate the size of the VLA primary beam which is  $8'$  at  $\lambda 6.2$  cm. The background optical image is from the DSS.

point-like source. This was accomplished by applying a procedure similar to the CLEAN algorithm by Högbom (1974). This procedure was revised and extended for application on single-dish observations by Klein and Rottmann (see Klein & Mack 1995; Rottmann 1996). The required beam patterns were obtained from deep observations of 3C 84 and 0234-23 at  $\lambda 3.6$  cm and  $\lambda 6.2$  cm, respectively. Each single map of NGC 253 was cleaned with the mean parallactic angle of the map, respectively. This is sufficient, since the variation of the parallactic angle is less than  $5^\circ$  during the observation of a single map.

We were able to obtain essentially noise limited maps with a dynamic range of at least 1000. The cleaned structures (the difference between the uncleaned and the cleaned map) exhibit prominent sidelobes extending far from the disk underlining the importance of a careful cleaning procedure. Details of the single-dish cleaning can be found in Heesen (2008).

## 2.2. The VLA observations

With the VLA<sup>3</sup> in D-configuration we observed NGC 253 in July 2004 at  $\lambda 6.2$  cm with a total integration time of 40 h. The size of the primary beam of the VLA antennas at  $\lambda 6.2$  cm is  $8'$ , requiring a mosaic of 15 pointings. They were arranged in three rows parallel to the major axis of the galaxy, including much of the extra-planar field of interest. An illustration of the mosaic setup is shown in Fig. 1 as an overlay onto an optical image from the DSS<sup>4</sup>. The data were calibrated with 3C 48 and 3C 138 as primary (flux) calibrators using the standard procedures in the Astronomical Image Processing System<sup>5</sup> with the flux density

<sup>3</sup> The VLA (Very Large Array) is operated by the NRAO (National Radio Astronomy Observatory).

<sup>4</sup> The compressed files of the “Palomar Observatory – Space Telescope Science Institute Digital Sky Survey” of the northern sky, based on scans of the Second Palomar Sky Survey are ©1993–1995 by the California Institute of Technology and are distributed herein by agreement.

<sup>5</sup> The Astronomical Image Processing System (AIPS) is distributed by the National Radio Astronomy Observatory (NRAO) as free software.

scale given in Baars et al. (1977). The performed self-calibration allowed us to suppress the sidelobes of the nuclear point-like source in order to gain a high dynamic range.

After inverting the  $(u,v)$ -data and the successive cleaning we convolved the maps of each pointing with a Gaussian in order to obtain an identical clean beam. Using LTESS (part of AIPS) the maps were finally combined with a linear superposition and a correction for the VLA primary beam attenuation using information from each pointing out to the 7% level of the primary beam (Braun 1988). Our final map has a noise level of  $30 \mu\text{Jy}/\text{beam}$  in total power which corresponds to a dynamic range of 40 000 with respect to the nucleus.

An important shortcoming of interferometric observations is the limited sensitivity to extended emission on large angular scales. The VLA in D-configuration at  $\lambda 6.2$  cm is only sensitive to emission with a scale smaller than  $5'$ . Since NGC 253 is much larger, we observe with the VLA only a fraction of the extended emission detected with a single-dish telescope. The influence of the missing zero-spacing flux density can be easily seen by comparing the Effelsberg map at  $\lambda 6.2$  cm in Fig. 3 with the VLA map shown in Fig. 2. The missing total flux density is about 10% of the total flux density measured with Effelsberg; if the flux density of the extended emission (without the nuclear point-like source) is considered, the fraction of the missing zero-spacing flux density increases to 20%.

We used the Effelsberg map in order to fill in the missing zero-spacing flux in the VLA map. This was done using IMERG (part of AIPS) which performs a Fourier combination of the two maps. We stress that in particular for mosaics, which cover the entire region of interest, a single-dish map is necessary in order to detect all extended emission.

The  $\lambda 90$  cm and  $\lambda 20$  cm maps are from VLA observations by Carilli et al. (1992). While one pointing with a primary beam size of  $138'$  is sufficient to cover NGC 253 at  $\lambda 90$  cm, three pointings with a beam size of  $25'$  were combined to a mosaic at  $\lambda 20$  cm. The largest angular scale structure which can be imaged reasonable well with the VLA is  $70'$  at  $\lambda 90$  cm and  $15'$  at  $\lambda 20$  cm, respectively. The needed correction for the missing zero-spacing flux of the mosaic at  $\lambda 20$  cm was not performed because no single-dish map is available at this wavelength. Hence, the  $\lambda 20$  cm map is not well suited to investigate the structure of the extended emission in the halo.

## 3. Morphology of the total power emission

We present the total power maps as contour plots with the first contour indicating emission at three times the rms noise level ( $3 \text{ rms} \times 2^{m-1}$ ;  $m = 1, 2, 3, \dots$ ). The optical background image was obtained from the DSS. A summary of the maps presented in this paper can be found in Table 1.

The continuum emission not only extends over the optical disk along the major axis, but we also find a notable extension of emission along the minor axis in all maps. We refer to this as *extra-planar* emission. A detailed analysis and proof that the emission does not belong to the disk is given in Sect. 5.1. The extent of extra-planar emission is strongly dependent on the observation wavelength, which can be seen by comparing the maps. The  $\lambda 90$  cm map shown in Fig. 4 has very pronounced extra-planar emission, while the disk does not show up prominently. The  $\lambda 20$  cm and  $\lambda 6.2$  cm maps presented in Figs. 5 and 6 have less extra-planar emission and at  $\lambda 3.6$  cm there is almost no extra-planar emission (Fig. 7).

The morphology of the total power emission also depends on the resolution and the sensitivity of the maps. In the  $\lambda 20$  cm

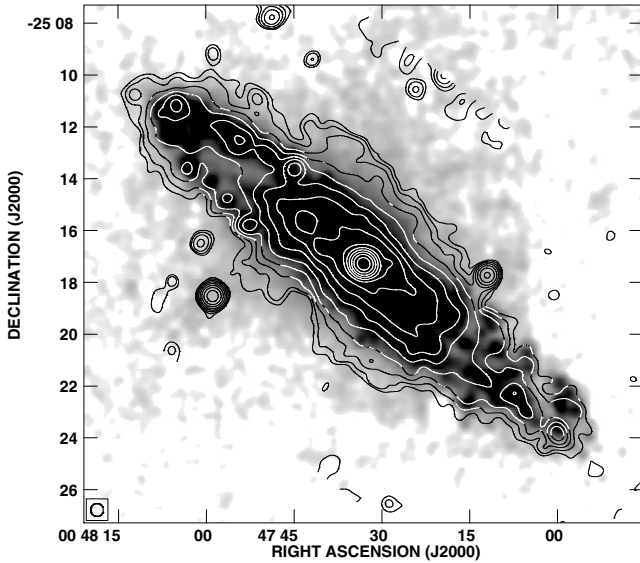


**Fig. 2.** Total power radio continuum at  $\lambda 6.2$  cm obtained from the VLA observations with  $30''$  resolution. Contours are at 3, 6, 12, 24, 48, 96, 192, 384, 768, 1536, 3077, 6144, 12 288, and  $24\,576 \times 30 \mu\text{Jy}/\text{beam}$ . The grey scale shows  $\text{H}\alpha$  emission from Hoopes et al. (1996).

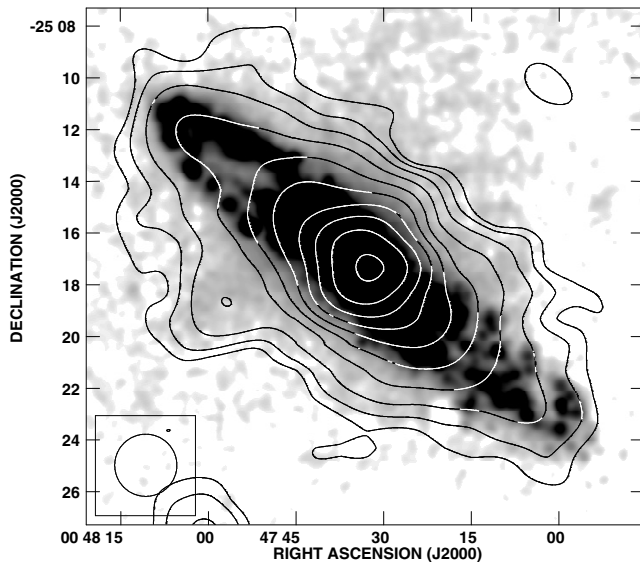


**Fig. 3.** Total power radio continuum at  $\lambda 6.2$  cm obtained from the Effelsberg observations with  $144''$  resolution. Contours are at 3, 6, 12, 24, 48, 96, 192, 384, 768, and  $1536 \times 1 \text{ mJy}/\text{beam}$ . The grey scale shows  $\text{H}\alpha$  emission as in Fig. 2.

and  $\lambda 6.2$  cm maps with a resolution of  $30''$  the spiral arms are distinct features in the disk, one extending to the northeast and another to the southwest. The inner part of the disk is visible as a plateau of high emission coinciding with the brightest part in the optical image. In all maps, independent of the resolution, there is an extension southeast of the nucleus with an unresolved source at its southern tip. This is an example of a so-called “radio spur”, where the magnetic field has a strong vertical component, as will be shown in Paper II.

The total extent of emission perpendicular to the disk is not a good measure for the amount of extra-planar emission since it depends on the sensitivity of the observations. This is visible in the  $\lambda 20$  cm map which shows less extra-planar emission than the  $\lambda 6.2$  cm map because its noise level is 10 times higher.

**Table 1.** The maps of NGC 253 included in this paper.

$\lambda$ [cm]	Resolution	rms [mJy/beam]	Dynamic range	References
90	$70''$	8	500	Carilli et al. (1992)
20	$30''$	0.35	5700	Carilli et al. (1992)
6.2	$30''$	0.03	42 000	this paper
3.6	$84''$	0.5	2000	this paper

Thus, with a low sensitivity we observe only the brightest tip of the radio halo. Moreover, the extent appears to be larger for low resolutions. This is the motivation to use the scaleheight  $h$  which prescribes the emission profiles perpendicular to the disk as an exponential function  $\propto \exp(-z/h)$  of the distance  $z$  from the galactic midplane. In Sect. 5.1 we discuss the scaleheights in order to characterize the radio halo.

We find that the extent of the extra-planar emission varies with the offset along the major axis. The contour lines in all maps show a dumbbell shape which means that the extension of the extra-planar emission has a local minimum at the center of the disk. While this trend is visible in all maps it is clearly seen at the shorter wavelengths. Especially the  $\lambda 3.6$  cm map has a prominent neck above and below the nucleus, where the contour lines indicate a steep gradient along the minor axis. This points to a smaller scaleheight of the extra-planar emission. If the scaleheight were constant along the major axis, the largest vertical extension of the emission would be expected in the center. We investigate this issue and give an explanation in Sect. 5.

## 4. Spectral index distribution

### 4.1. Unresolved sources

Our continuum maps, in particular those with the highest resolution, show several unresolved (point-like) sources. We identified the sources in order to subtract them from the maps prior to our analysis of the extended emission. We obtained peak flux densities and positions by fitting Gaussians to them, where we corrected the peak flux density for the underlying extended emission. This is particularly important for the nuclear point-like source, because it is embedded in strong extended emission. The list of point-like sources presented in Table 2 includes positions, flux densities, and spectral indices. The spectral  $\alpha$  is defined by the relation  $S \propto \nu^{-\alpha}$ , where  $S$  is the total power radio continuum flux density and  $\nu$  is the observation frequency. The strongest two sources, the nucleus (No. 3) and the source in the radio spur (No. 6), are detected at all four wavelengths. For these two sources the spectral index and its error is calculated in the range between  $\lambda 90$  cm and  $\lambda 3.6$  cm. Point source No. 6 was resolved with VLA observations in B-configuration into two components with  $2''$  separation (Carilli et al. 1992). This source that has no known optical counterpart is likely a background AGN.

### 4.2. Total flux density

The total radio continuum flux density was integrated within ellipses with the major axis aligned to the position angle ( $\text{PA} = 52^\circ$ ) of NGC 253. The ellipses were chosen such that the visible extended emission in the disk and halo is covered. The parameters of the flux density integration are listed in Table 3 and the total flux densities obtained at different measurements are listed in Table 4. The flux densities of the point-like sources were

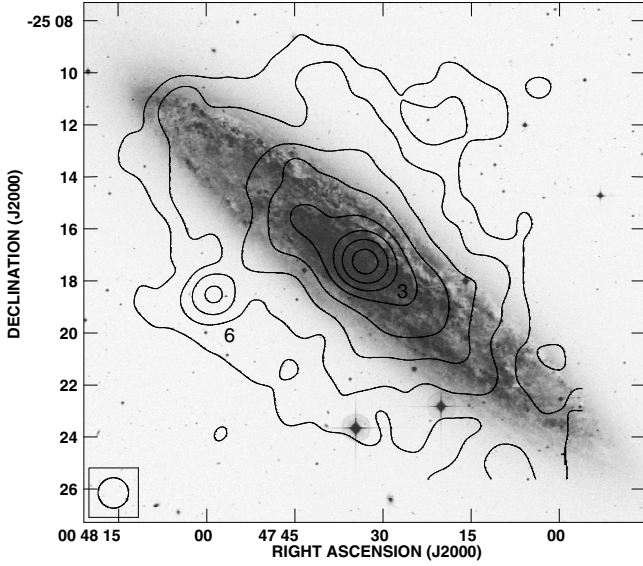


**Fig. 4.** Total power radio continuum at  $\lambda 190$  cm obtained from VLA observations with  $70''$  resolution. Contours are at 3, 6, 12, 24, 48, 96, 192, 384, 768, 1536, and  $3077 \times 8$  mJy/beam. The map is reproduced from Carilli et al. (1992).

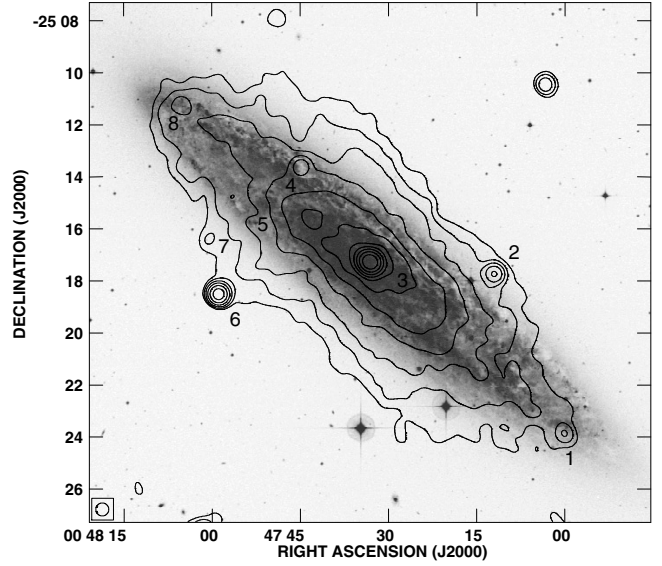


**Fig. 5.** Total power radio continuum at  $\lambda 120$  cm obtained from VLA observations with  $30''$  resolution. Contours are at 3, 6, 12, 24, 48, 96, 192, 384, 768, 1536, and  $3077 \times 0.35$  mJy/beam. The map is reproduced from Carilli et al. (1992).

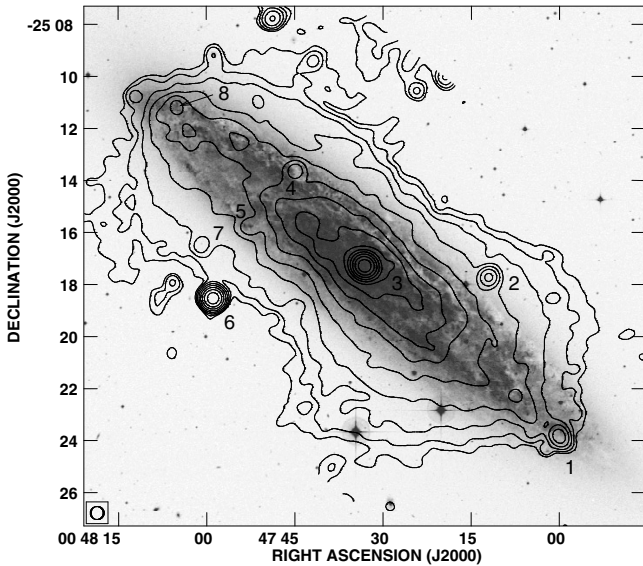


**Fig. 6.** Total power radio continuum at  $\lambda 16.2$  cm obtained from combined VLA and Effelsberg observations with  $30''$  resolution. Contours are at 3, 6, 12, 24, 48, 96, 192, 384, 768, 1536, 3077, 6144, 12 288, and  $24 576 \times 30 \mu\text{Jy}/\text{beam}$ .

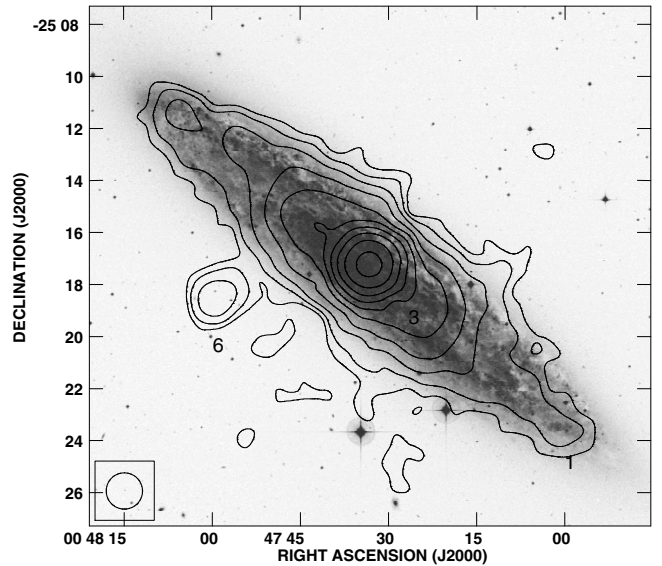


**Fig. 7.** Total power radio continuum at  $\lambda 13.6$  cm obtained from Effelsberg observations with  $84''$  resolution. Contours are at 3, 6, 12, 24, 48, 96, 192, 384, 768, and  $1536 \times 0.5$  mJy/beam.

subtracted from the total flux density, in order to obtain the flux density of the extended emission only.

The average spectral index of the extended emission is  $\alpha_e = 0.90 \pm 0.08$  in the range between  $\lambda 90$  cm and  $\lambda 13.6$  cm. This spectrum is considerably steeper than that of young cosmic ray electrons (CREs) in supernova remnants (SNRs) with  $\alpha \approx 0.5$ , although young shell SNRs can have a steeper spectrum with  $\alpha \approx 0.7$  (see e.g. Green 2002). This is an indication for synchrotron losses of the CREs, which is discussed in Sect. 5.3.

Assuming a thermal fraction of 8% at  $\lambda 120$  cm (Niklas et al. 1997), we find a synchrotron non-thermal spectral index of  $\alpha_{nt} = 1.0$ .

#### 4.3. Extended emission

In this section we present the spectral index distribution of the extended emission, which we obtained from the total power maps. The center of all spectral index maps is dominated by the nuclear point-like source (No. 3) with its flat spectral index of  $\alpha = 0.44$ . In Fig. 8 we present the  $\lambda 90$  cm/ $\lambda 120$  cm spectral index map. The  $\lambda 120$  cm map was convolved with a Gaussian to match the resolution of the  $\lambda 90$  cm map with  $70''$ . At this low resolution the inner disk and the spiral arms are not resolved. We find that the spectral index gradually steepens with increasing distance from the major axis, with the gradient strongest in the inner part of the disk. There is a slight trend that indicates that the southwestern part possesses a flatter spectral index than the northeastern part. At the southern tip of the radio spur the

**Table 2.** Unresolved sources which are denoted in Figs. 4–7. The error of the flux densities was calculated assuming a 5% calibration error.

No.	RA	Dec	$S_{\lambda 90}$ [mJy]	$S_{\lambda 20}$ [mJy]	$S_{\lambda 6.2}$ [mJy]	$S_{\lambda 3.6}$ [mJy]	$\alpha$
1	00 <sup>h</sup> 47 <sup>m</sup> 00 <sup>s</sup> .02	−25°23′50″.1		4.1 ± 0.2	2.2 ± 0.1		0.5 ± 0.2
2	00 <sup>h</sup> 47 <sup>m</sup> 12 <sup>s</sup> .01	−25°17′43″.9		17.3 ± 1.0	6.6 ± 0.3		0.8 ± 0.2
3	00 <sup>h</sup> 47 <sup>m</sup> 33 <sup>s</sup> .12	−25°17′17″.3	3960 ± 80	2040 ± 100	1270 ± 60	980 ± 50	0.44 ± 0.02
4	00 <sup>h</sup> 47 <sup>m</sup> 44 <sup>s</sup> .91	−25°13′38″.4		26 ± 2	7.9 ± 0.4		1.0 ± 0.2
5	00 <sup>h</sup> 47 <sup>m</sup> 52 <sup>s</sup> .41	−25°15′44″.8			1.5 ± 0.2		
6	00 <sup>h</sup> 47 <sup>m</sup> 58 <sup>s</sup> .90	−25°18′31″.9	190 ± 10	53 ± 3	19 ± 1	9.5 ± 0.5	0.84 ± 0.02
7	00 <sup>h</sup> 48 <sup>m</sup> 00 <sup>s</sup> .84	−25°16′26″.3		2.1 ± 0.3	1.10 ± 0.06		0.5 ± 0.2
8	00 <sup>h</sup> 48 <sup>m</sup> 05 <sup>s</sup> .0	−25°11′11″.8		5.3 ± 0.3	3.05 ± 0.15		0.4 ± 0.2

**Table 3.** The total flux densities were integrated within ellipses chosen to include the extended emission in the disk and halo. The major axis  $a$ , and the minor axis  $b$  for each wavelength  $\lambda$  is presented.

$\lambda$ [cm]	$a$ [arcsec]	$a$ [kpc]	$b$ [arcsec]	$b$ [kpc]
90	620	12.1	392	7.6
20	620	12.1	392	7.6
6.2	680	13.3	430	8.4
3.6	648	12.6	400	7.8

**Table 4.** Integrated total power flux densities.  $S_i$  is the total integrated flux density and  $S_e$  is the flux density of the extended emission only. The error of the flux densities was calculated as the quadratic sum of a 5% calibration error and the baselevel error.

$\lambda$ [cm]	Instrument	$S_i$ [Jy]	$S_e$ [Jy]
90	VLA	16.5 ± 1.9	12.5 ± 1.9
20	VLA	6.3 ± 1.1	4.2 ± 1.1
6.2	VLA + Effelsberg	2.71 ± 0.14	1.44 ± 0.07
3.6	Effelsberg	1.66 ± 0.08	0.68 ± 0.04

point-like source No. 6 is recognized by its flatter spectral index of  $\alpha = 0.84$  compared with the spectral index in the halo.

The  $\lambda 20$  cm/ $\lambda 6.2$  cm spectral index map presented in Fig. 9 with its higher resolution of 30'' reveals more details. The spiral arms are well resolved and show a flatter spectral index than the inter-arm regions. In addition the inner disk has a notable plateau with a flat spectral index of 6' extent along the major axis, which is not so clearly seen in the other maps. We find regions of steep spectral index ( $\alpha > 1$ ) at the base of the radio spur and at the northeastern extension. This finding agrees with the  $\lambda 90$  cm/ $\lambda 20$  cm spectral index map presented above, which has a steep spectral index at these locations, too.

The  $\lambda 90$  cm/ $\lambda 3.6$  cm spectral index map presented in Fig. 10 has the lowest angular resolution of 84'' among our spectral index maps. The morphology of this map is similar to the  $\lambda 20$  cm/ $\lambda 6.2$  cm map even though smoothed out in comparison. The spectral index is flat in the inner disk and in the spiral arms with  $\alpha < 0.7$ . Limited by the sensitivity of the  $\lambda 3.6$  cm map we find only four small extensions with extra-planar spectral indices, which are steeper than in the disk. The exception is the extension northwest of the nucleus, which contains the point-like source No. 2 with a flat spectral index of  $\alpha = 0.68$ .

## 5. Cosmic ray transport

While the CRs are created and accelerated in the disk, the observation of extra-planar radio continuum emission requires a

transport of CRs from the disk into the halo. This transport is investigated in this section.

### 5.1. The scaleheight of the thick radio disk

With the observed inclination angle of  $i = 78.5^\circ \pm 0.5^\circ$  (Pence 1980) any emission profile taken perpendicular to the disk is a superposition of disk and halo emission. We created a template of the vertical emission profile by projecting the emission profile along the major axis onto the minor axis. Moreover, the profile was convolved to the resolution of the observations in order to account for the beam smearing. Thus, the *effective beam size* was determined by fitting a Gaussian to the resulting profile. Any emission profile perpendicular to the disk that does not exceed the effective beam size cannot be attributed to extra-planar emission but is just the observed inclined emission of the disk. Hence, we arrived at effective beam sizes of 1.2', 1.2', 2.1', and 2.5' for  $\lambda 90$  cm,  $\lambda 20$  cm,  $\lambda 6.2$  cm, and  $\lambda 3.6$  cm, respectively.

For the following analysis of the extended emission we subtracted all point-like sources by fitting Gaussians to them. The emission profiles were obtained using a strip integration perpendicular to the major axis with a strip width of 1.5' (1.7 kpc) and a pixel separation of 0.25' (0.29 kpc). With the routine discussed in Dumke et al. (1995) profiles consisting of two exponential functions were fitted to the measured profiles taking the effective beam size into account. This yields a scaleheight of the thin and the thick radio disks for the northern and the southern hemisphere, respectively. The synchrotron scaleheight  $h_{\text{syn}}$  is calculated as the mean of the scaleheight of the thick radio disk in the northern and the southern hemisphere. In case we could not obtain a two-component fit, we took the one-component exponential scaleheight as the thick radio disk.

The scaleheights are smallest in the center and increase along the major axis further away from the center. This is shown in Fig. 11 where also the variations of the total magnetic field strength and the CRE lifetime are presented. The error of the scaleheights is estimated by varying the choice of data points. Moreover, the difference between the northern and the southern scaleheights contributes to the error. The weighted mean scaleheight at  $\lambda 6.2$  of the thin radio disk is  $0.33' \pm 0.05'$  ( $0.38 \pm 0.06$  kpc). The thick radio disk at  $\lambda 6.2$  cm has a scaleheight of  $1.5' \pm 0.1'$  ( $1.7 \pm 0.1$  kpc). At  $\lambda 20$  cm scaleheights of  $0.38' \pm 0.05'$  ( $0.44 \pm 0.06$  kpc) for the thin radio disk and  $1.5' \pm 0.1'$  ( $1.7 \pm 0.1$  kpc) for the thick radio disk are found. Note that the  $\lambda 20$  cm profiles drop beyond 3' height above the disk due to missing large-scale structure. However, this has only a marginal effect on the scaleheights.

The  $\lambda 6.2$  cm and  $\lambda 20$  cm maps have a sufficient signal-to-noise (S/N) ratio, so that we were able to obtain two-component exponential distributions, whereas the  $\lambda 3.6$  cm map does not

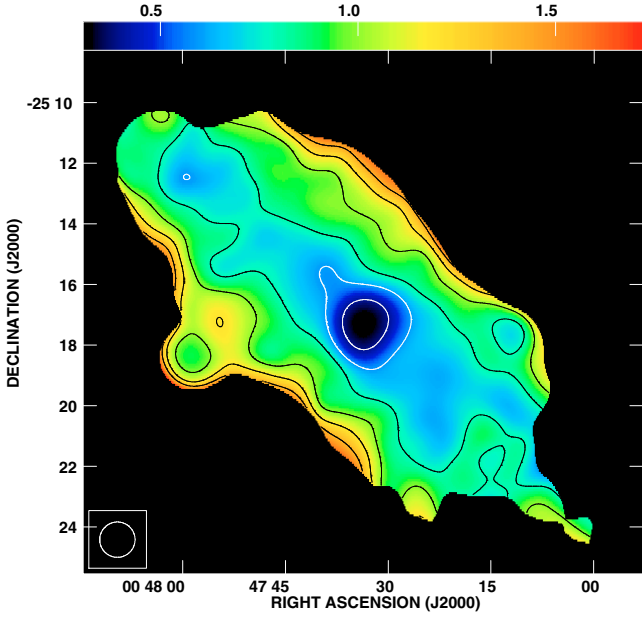


**Fig. 8.** Spectral index distribution between  $\lambda 190$  cm and  $\lambda 120$  cm with  $70''$  resolution. Contours are at 0.6, 0.8, 1.0, 1.2, and 1.4. The total power radio continuum maps were clipped at a level of  $4\times$  the rms noise prior to the combination, resulting in a spectral index error of less than  $\pm 0.3$ .

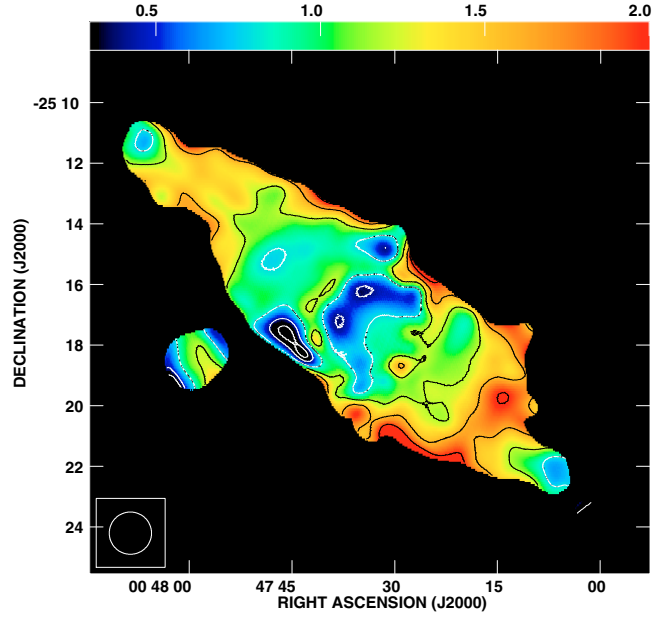


**Fig. 10.** Spectral index distribution between  $\lambda 16.2$  cm and  $\lambda 13.6$  cm with  $84''$  resolution. Contours are at 0.2, 0.4, 0.8, 1.2, 1.6, and 2.0. Both total power radio continuum maps were clipped at a level of  $7\times$  the rms noise prior to the combination, resulting in a spectral index error of less than  $\pm 0.5$ .

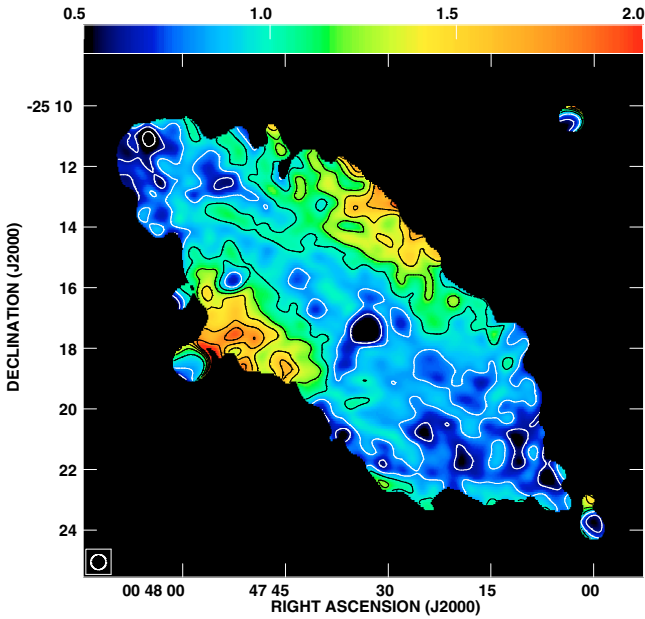


**Fig. 9.** Spectral index distribution between  $\lambda 120$  cm and  $\lambda 16.2$  cm with  $30''$  resolution. Contours are at 0.6, 0.8, 1.0, 1.2, 1.4, 1.6, and 1.8. Both total power radio continuum maps were clipped at a level of  $5\times$  the rms noise prior to the combination, resulting in a spectral index error of less than  $\pm 0.4$ .

have a sufficient S/N ratio so that we used only a one-component exponential distributions. At  $\lambda 13.6$  cm we found a mean scaleheight of  $0.5' \pm 0.1'$  ( $0.6 \pm 0.1$  kpc) and at  $\lambda 190$  cm we found  $2.2' \pm 0.2'$  ( $2.5 \pm 0.2$  kpc). The scaleheights at  $\lambda 13.6$  cm are dominated by the thin disk, because the low signal does not allow the thick disk to be traced to sufficiently large distances. In contrast at  $\lambda 190$  cm the emission is dominated by the thick radio disk so that one-component exponential fits are sufficient.

The average scaleheight of NGC 253 agrees well with those reported for other edge-on galaxies at  $\lambda 16$  cm (see also Sect. 6). That the scaleheight of the thick radio disk is larger than the effective beam proves the finding of extra-planar emission and hence the existence of a radio halo. The scaleheights of the thick disk at  $\lambda 16.2$  cm,  $\lambda 120$  cm, and  $\lambda 190$  cm are smallest for the central strips where the underlying SFR is highest. This important observation is the result of synchrotron loss and is discussed in the next sections.

## 5.2. The total magnetic field strength

From the non-thermal total power emission one can determine the total magnetic field strength assuming equipartition between the energy density of the CRs and the magnetic field. Here we used the revised equipartition formula by Beck & Krause (2005) assuming a pathlength of 6.5 kpc, which is the full width to the half power of the Gaussian fitted to the total power emission along the major axis. Moreover, we assumed a non-thermal spectral index of  $\alpha_{nt} = 1.0$  (see Sect. 4.2), a fractional polarization of 5.5% (see Paper II), and a number density ratio  $K_0 = 100$  of protons and electrons. We stress that the last assumption might not be well fulfilled at large distances from the disk, because the CREs suffer high synchrotron losses whereas the CR protons are almost unaffected. Hence, the observed  $K$  factor increases with increasing distance from the CR sources which are located in the disk. The magnetic field strength is then underestimated by a small factor of  $(K/K_0)^{1/4}$  (Beck & Krause 2005).

The structure of the regular magnetic field in NGC 253 is a superposition of a disk and a vertical component (see Paper II). The disk component is a spiral with a constant pitch angle and the inclination angle of the optical disk. The vertical component is orientated perpendicular to the disk. The above presented parameters as well as the geometry of the magnetic field were assumed to be constant when computing the total magnetic field

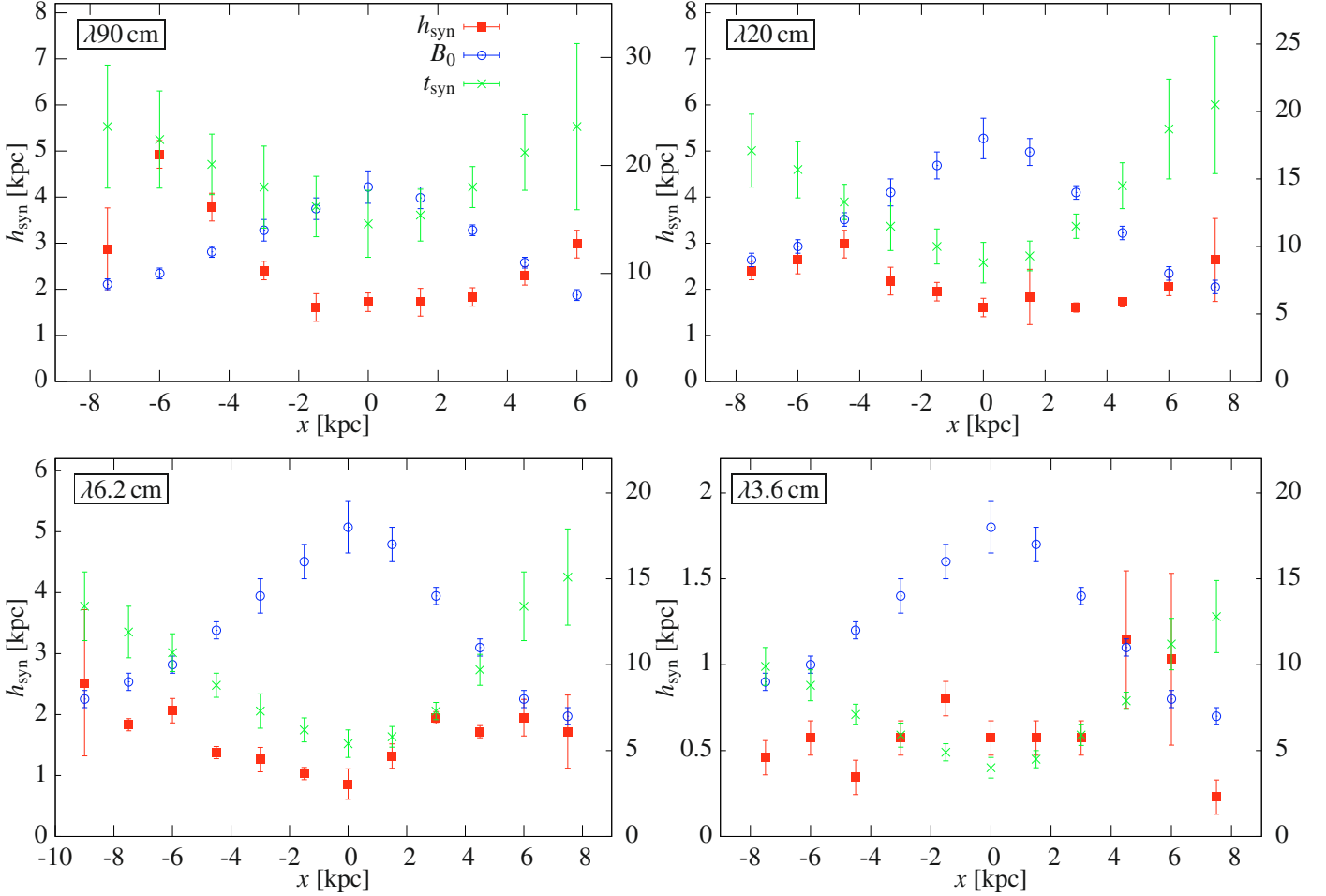


**Fig. 11.** Scaleheight  $h_{\text{syn}}$  as a function of the offset  $x$  along the major axis (northeast is positive and southwest is negative). The magnetic field strength  $B_0$  (in units of  $\mu\text{G}$  on the right axis) and the electron lifetime  $t_e$  (in units of  $10^6$  yr on the right axis) are also shown.

strength. To check the sensitivity of this assumption we varied the parameters in a certain range and observed its influence on the total magnetic field strength. We used an integration path length between 5 kpc and 20 kpc, a fractional polarization between 5% and 20%, a non-thermal spectral index between 0.8 and 1.2, and assumed two structures for the magnetic field: disk-parallel or vertical. The former one describes the geometry of the magnetic field structure in the disk, where all possible magnetic field directions along the line of sight are taken into account. The latter one describes the geometry of the magnetic field in the halo, where a constant magnetic field direction along the line of sight is assumed. The variation of the total magnetic field strength in this range of conditions was found to be  $1.5 \mu\text{G}$ , which we thus adopt as an estimate for the systematic error of the total magnetic field strength.

The total magnetic field strength was scaled with the non-thermal synchrotron intensity  $I_n$  using the standard equipartition formula (Beck & Krause 2005):

$$B \propto I_n^{1/(3+\alpha_{\text{nt}})}. \quad (1)$$

The distribution of the total magnetic field strength shown in Fig. 13 was calculated from the  $\lambda 6.2$  cm map. It ranges between  $7 \mu\text{G}$  and  $18 \mu\text{G}$  in the disk and is smaller in the halo. Note the subtracted nucleus, which is highlighted by a notable residual hole in the center of the map. The strip integration as described

above applied to the map of the total magnetic field strength was used in order to find the maximum of the total magnetic field strength  $B_0$  in each strip. This gives a lower limit on the lifetime of the CREs as described in the next section.

Thompson et al. (2006) argued that the magnetic field strength in starburst galaxies may be underestimated using the equipartition value. Our measured mean magnetic field strength of  $12 \mu\text{G}$  in the disk is accurately in equipartition with the mean gas surface-density  $\Sigma_g = 0.84 \times 10^{-2} \text{ g cm}^{-2}$  (Puche et al. 1991), so that the disk of NGC 253 fits onto the equipartition line, although its starburst nucleus does not (see Fig. 1 in Thompson et al. 2006).

### 5.3. Loss processes of the cosmic ray electrons

Several processes are known through which the CREs lose energy, like synchrotron radiation, inverse Compton (IC) losses, non-thermal bremsstrahlung, ionization losses, and adiabatic losses. They all have different timescales which determine the lifetimes of the CREs. In order to calculate the timescales we adopt the equations by Pohl (1990). The synchrotron lifetime of CREs is

$$t_{\text{syn}} = 8.352 \times 10^9 E(\text{GeV})^{-1} B(\mu\text{G})^{-2} \text{ yr}, \quad (2)$$

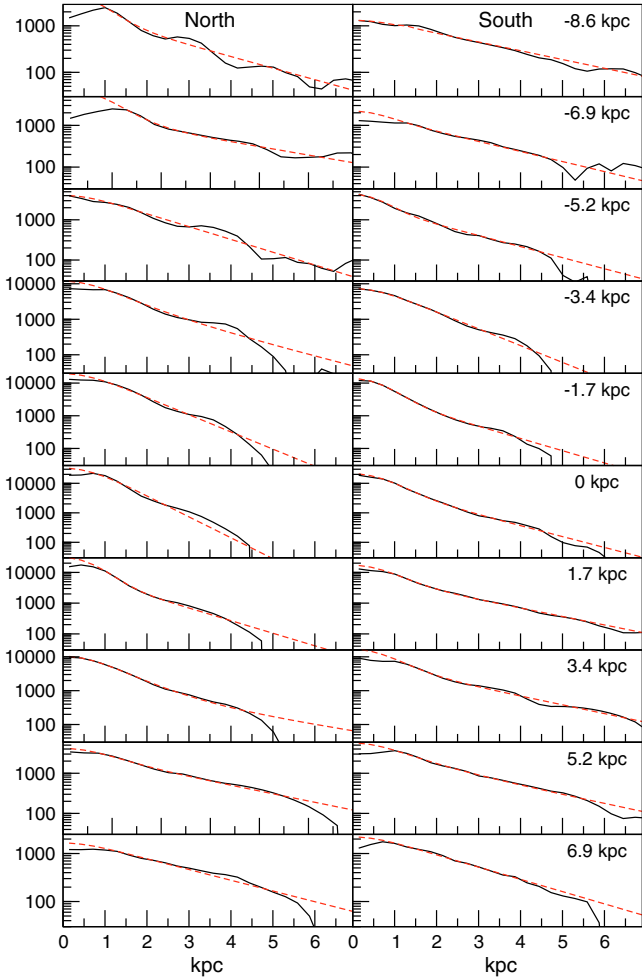


**Fig. 12.** Total power emission profiles in  $\mu\text{Jy}/\text{beam}$  at  $\lambda 6.2$  cm perpendicular to the disk. The solid line shows the measured profile and the dashed line shows the fitted profile consisting of two exponential functions convolved with the effective beam. The offset of the profiles along the major axis is denoted.

where  $E$  is the CRE energy and  $B$  is the total magnetic field strength. In the following we use the relation between the CRE energy  $E$ , the observation frequency  $\nu$ , and the total magnetic field strength  $B$  (Rybicki & Lightman 1986):

$$E(\text{GeV}) = (\nu/(16.1 \text{ MHz}))^{1/2} B(\mu\text{G})^{-1/2}. \quad (3)$$

For the  $\lambda 6.2$  cm observations with  $\nu = 4860$  MHz and a typical magnetic field strength of  $15 \mu\text{G}$  we find  $E = 4.5$  GeV and hence  $t_{\text{syn}} = 8.2 \times 10^6$  yr. Inverse Compton (IC) radiation losses have the same energy dependence as synchrotron losses and the corresponding lifetime is

$$t_{\text{IC}} = 3.55 \times 10^8 (E(\text{GeV}))^{-1} (U_{\text{ph}}/(10^{-12} \text{ erg cm}^{-3}))^{-1} \text{ yr}, \quad (4)$$

where  $U_{\text{ph}}$  is the total photon energy density. From the infrared observations of Radovich et al. (2001) we find a total photon energy density of  $1.3 \times 10^{-12} \text{ erg cm}^{-3}$  which leads to  $t_{\text{IC}} = 6.1 \times 10^7$  yr. This is almost an order of magnitude larger than the synchrotron lifetime.

For the non-thermal CRE bremsstrahlung lifetime we use

$$t_{\text{brems}} = 3.96 \times 10^7 n(\text{cm}^{-3})^{-1} \text{ yr}, \quad (5)$$

where  $n$  is the ISM gas density. The ionization losses lead to a CRE lifetime of:

$$t_{\text{ion}} = 9.5 \times 10^6 n(\text{cm}^{-3})^{-1} E(\text{GeV}) \text{ yr}. \quad (6)$$

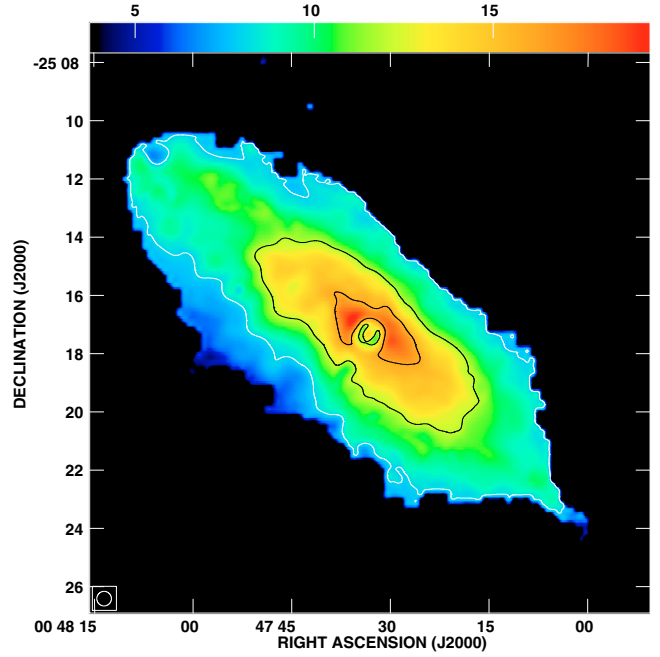


**Fig. 13.** Map of the total magnetic field strength with a resolution of  $30''$ . Contours are at  $8, 12,$  and  $16 \times 1 \mu\text{G}$ .

We now use a mean gas column density of  $\Sigma_{\text{g}} = 4 M_{\odot} \text{ pc}^{-2}$  for the total gas as determined by Puche et al. (1991) from HI observations. We define a cylinder with the diameter of the disk  $D_{25} = 27.7'$  (31.7 kpc) and adopt a height of 3.4 kpc which is twice the scaleheight of the thick radio disk. The mean density of  $\rho = 7.9 \times 10^{-26} \text{ g cm}^{-3}$  or  $n \approx 0.05 \text{ cm}^{-3}$  leads to a bremsstrahlung lifetime of  $t_{\text{brems}} = 8 \times 10^8$  yr and an ionization lifetime of  $t_{\text{ion}} = 8.6 \times 10^8$  yr.

The adiabatic timescale

$$t_{\text{ad}} = 3 \left( \frac{d\theta}{dz} \right)^{-1}. \quad (7)$$

depends only on the reciprocal velocity gradient. At this point we do not have any information about the velocity profiles. We estimate, however, the timescale of the adiabatic losses in Sect. 5.5 as  $3.6 \times 10^7$  yr, so that the synchrotron losses and the adiabatic losses are the most important loss processes of the CREs.

The local synchrotron lifetime calculated with Eq. (2) may be an overestimate, because we observe at a certain location the superposition of locally produced CRs and CRs, which were transported there from their origins. The latter ones have already lost a fraction of their energy and have shorter lifetimes than indicated by the local synchrotron losses. This effect is large in the halo, where almost all CRs were transported away from their origins. In the disk, where we observe the highest fraction of locally produced CRs, this effect is small. Hence, we used the minimum of the local synchrotron lifetime  $t_{\text{syn},0}$  calculated from the maximum magnetic field strength  $B_0$  in the disk as the most accurate estimate.

Because  $B$  decreases with  $z$ ,  $t_{\text{syn},0}$  is an underestimate. An improved estimate needs integration over the  $B$  profile, which is, however, not known well enough. As a starting point we assume an exponential vertical profile. As shown in Appendix A we find in this case that  $t_{\text{syn},0}$  is overestimated by no more than 10% if we restrict the data to  $z < h_{\text{syn}}$ .

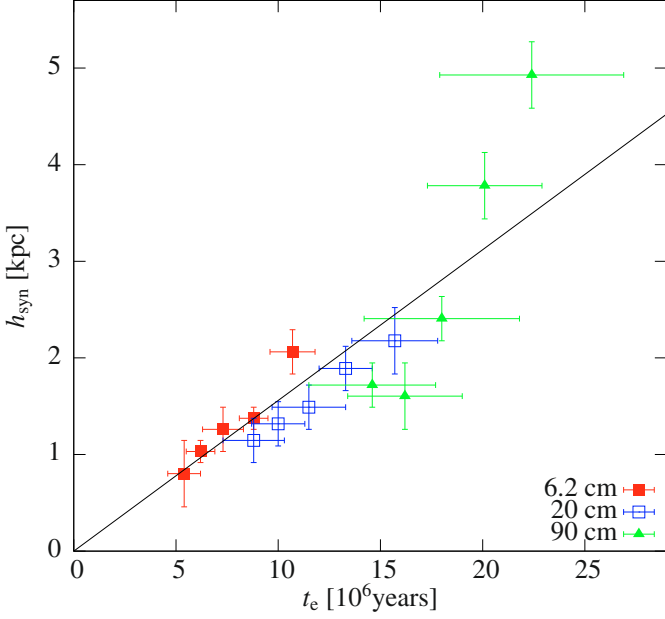


**Fig. 14.** Scaleheight  $h_{\text{syn}}$  of the thick radio disk as a function of the CRE lifetime  $t_e$  in the northeastern halo (between  $-6$  kpc and  $0$  kpc offset along the major axis). The linear fit is the theoretical expectation for a convective CR transport with a constant CR bulk speed.

Summarizing this section, the CRE energy loss is dominated by the synchrotron radiation and the adiabatic losses. Hence, we have to combine the two energy losses in order to estimate the lifetime  $t_e$  of the CREs, using:

$$\frac{1}{t_e} = \frac{1}{t_{\text{syn},0}} + \frac{1}{t_{\text{ad}}}. \quad (8)$$

Since the adiabatic time scale is constant, the CRE lifetime is a function of the synchrotron lifetime. This can be seen in Fig. 11, where we show the variation of  $B_0$  and  $t_e$  along the major axis. The magnetic field strength has its maximum in the center of the disk where both the synchrotron lifetime and the CRE lifetime have a minimum.

#### 5.4. The cosmic ray bulk speed

As described in Sect. 3 the total power emission resembles a dumbbell shape at all observed wavelengths; the contour lines show a strong thinning in the center close to the nucleus at the brightest part of the disk. The analysis of the scaleheight of the thick radio disk confirms this morphological analysis: it increases with galactocentric radius with the minimum at the strip centered on the nucleus. The opposite behavior is found for the magnetic field strength, which decreases from the center to the outer part of the disk. Hence, the scaleheight is small where the synchrotron lifetime  $t_{\text{syn},0}$  and hence the CRE lifetime  $t_e$  is small and vice versa.

This relation motivates to calculate the average CR bulk speed,

$$v = \frac{h_e}{t_e}, \quad (9)$$

where  $h_e$  is the CRE scaleheight. Inserting the non-thermal synchrotron intensity  $I_n \propto \exp(-z/h_{\text{syn}})$  into Eq. (1) and using the

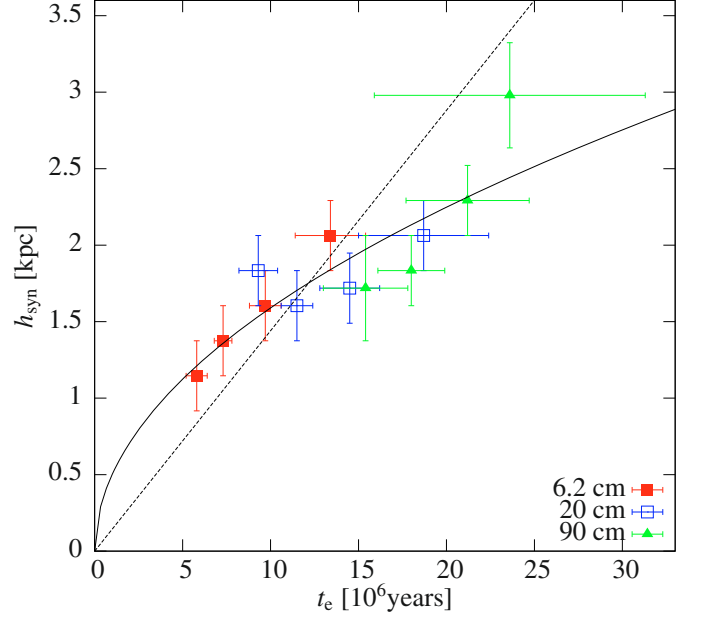


**Fig. 15.** Same as Fig. 14 in the southwestern halo (between  $1.5$  kpc and  $6$  kpc offset along the major axis). The linear fit (dashed line) is the theoretical expectation for a convective CR transport with a constant CR bulk speed, while the square root fit (solid line) is for a diffusive CR transport (see text for details).

equipartition condition  $n_e \propto B^2$  we find for the exponential profile of the CRE number density

$$n_e \propto \left\{ \exp\left(\frac{-z}{h_{\text{syn}}}\right) \right\}^{\frac{2}{3+\alpha_{\text{nt}}}}, \quad (10)$$

where  $h_{\text{syn}}$  is the synchrotron scaleheight of the thick radio disk. Thus, the CRE scaleheight is:

$$h_e = \frac{3 + \alpha_{\text{nt}}}{2} h_{\text{syn}}. \quad (11)$$

Since  $\alpha_{\text{nt}} = 1$  the CRE scaleheight is twice the scaleheight of the thick radio disk.

In Fig. 14 the scaleheight of the thick radio disk at  $\lambda 90$  cm,  $\lambda 20$  cm, and  $\lambda 6.2$  cm is shown for each strip as a function of the CRE lifetime. We find a (roughly) linear dependence between  $h_{\text{syn}}$  and  $t_e$ . The CR bulk speed in the northeastern halo is  $300 \pm 30$  km s $^{-1}$ , where the error is dominated by the uncertainty in the magnetic field strength and thus in the electron lifetime. The linear least square fit has a reduced  $\chi^2 = 3.6$ . In the southwestern halo, we find a flatter dependence between the scaleheight and the CRE lifetime (Fig. 15) with a CR bulk speed of  $250 \pm 30$  km s $^{-1}$  with a ( $\chi^2 = 2.7$ ). In this part of the halo the scaleheight can be better fitted by square root function ( $\chi^2 = 0.8$ ).

In the northeastern halo, the CR bulk speed is constant between  $\lambda 90$  cm and  $\lambda 6.2$  cm and does not vary with the CRE lifetime. This can be explained by a convective CR transport, where the CRs and the magnetized ISM are transported together. In this case, the CR bulk speed is independent of the CR energy and hence in the northeastern halo the CR transport is probably dominated by convection.

In the southwestern halo, the CR bulk speed decreases with increasing CRE lifetime and increasing wavelength. This can be explained by a diffusive CR transport where the CR bulk speed is  $v \approx \kappa / (\Gamma_c \cdot h_e)$ . Here,  $\kappa$  is the diffusion coefficient and  $\Gamma_c = 4/3$  is the adiabatic index of the relativistic CR gas. Replacing the

electron scaleheight by  $h_e = v \cdot t_e$  we obtain  $v \approx \sqrt{\kappa/(\Gamma_c \cdot t_e)}$ . Since the diffusion coefficient is usually assumed to increase with the CR energy ( $\kappa \propto E^{0.5}$ ), the CR bulk speed decreases both with increasing wavelength and with increasing synchrotron lifetime. This agrees with our observations and hence in the southwestern halo diffusion probably plays a significant role. Using the square root fit of Fig. 15 we find a diffusion coefficient of  $\kappa = (2.0 \pm 0.2) \times 10^{29} \text{ cm}^2 \text{ s}^{-1}$  which is in the range of the values quoted by Breitschwerdt et al. (1993).

The relation between the scaleheight and the CRE lifetime explains the observed pattern of the dumbbell total power emission. In the center of the galaxy the magnetic field strength is highest and hence the synchrotron lifetime is smallest; it hampers the transport of CREs into the halo. This effect even overcomes the excess of emission in the center. The contour lines thus show a steep gradient in the center above and below the nucleus.

### 5.5. Adiabatic losses

Using the information about the CR transport we can now calculate the adiabatic loss timescale mentioned in Sect. 5.3. The CRs are accelerated to their bulk speed of  $300 \text{ km s}^{-1}$  within the CRE scaleheight of 3.6 kpc. The adiabatic timescale is thus  $t_{\text{ad}} = 3.6 \times 10^7 \text{ yr}$  using Eq. (7), assuming a constant acceleration. This timescale is similar to the synchrotron lifetime of the CREs. Hence, the adiabatic losses have to be considered in particular for the low-energy CREs emitting at  $\lambda 90 \text{ cm}$ . A transition of adiabatic loss dominated CR transport to radiative dominated CR transport should be visible in the spectrum as a steepening from a flat spectral index at low frequencies to a steep spectral index at high frequencies (Pohl & Schlickeiser 1990). The break in the spectrum with a steepening of  $\Delta\alpha = 0.5$  occurs at the frequency where the adiabatic losses are equal to the radiation losses.

Since the CR transport is different for the northeastern and southwestern halo it is worthwhile to investigate the spectra of the extended flux density in these regions separately. For this we integrated the flux density in three boxes with a width of 5.2 kpc and a height of 5.7 kpc and an offset of  $-5.2 \text{ kpc}$ ,  $0 \text{ kpc}$ , and  $5.2 \text{ kpc}$  along the major axis. The corresponding spectra in Fig. 16 steepen to higher frequencies in particular the spectrum of the central region. This indicates high adiabatic losses at  $\lambda 90 \text{ cm}$ . From linear fits we derive the spectral index as  $0.97 \pm 0.05$ ,  $0.82 \pm 0.05$ , and  $0.89 \pm 0.05$  in the northeastern, central, and southwestern halos, respectively.

### 5.6. Cosmic ray spectral aging

In the previous section we calculated the CR bulk speed from the scaleheight of the CRE and their lifetime. Since the radiation power of the synchrotron emission is proportional to  $E^2$ , the spectral index steepens with time. This so-called CR *spectral aging* can be used for an alternative approach to calculate the CR bulk speed as we show in this section.

A single CRE loses its energy via synchrotron radiation with a loss power of

$$\frac{dE}{dt} = -\frac{\sigma_T c B_0^2}{8\pi} \left(\frac{E}{mc^2}\right)^2, \quad (12)$$

where  $\sigma_T = 6.65 \times 10^{-25} \text{ cm}^2$  is the Thomson cross section,  $B_0$  is the (constant) total magnetic field strength, and  $m = 511 \text{ keV}/c^2$  is the electron rest mass. The time dependence of

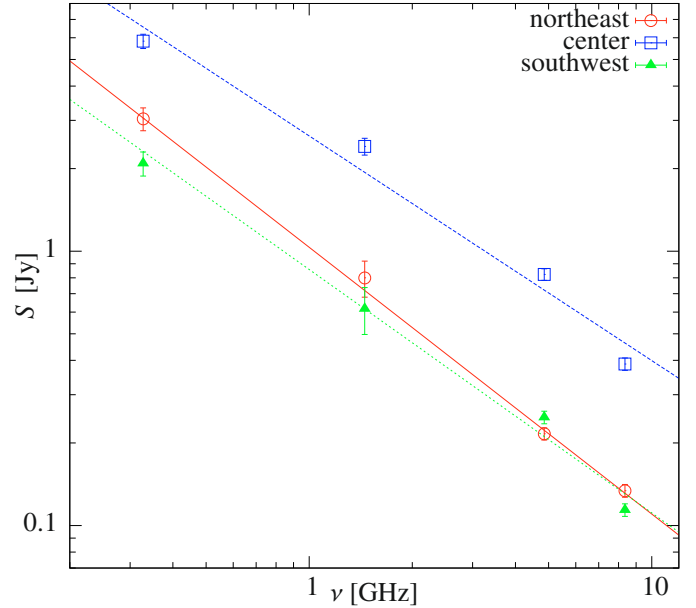


Fig. 16. Spectra of the diffuse emission in the northeastern halo, the central halo, and the southwestern halo.

the CRE energy is  $E(t) = E_0/(1 + t/t_{\text{syn}})$ , where the synchrotron lifetime  $t_{\text{syn}}$  is the time where a CRE has lost half of its initial energy  $E_0$ .

The electron spectral index is defined by

$$\gamma = -\log \frac{N_1}{N_2} \bigg/ \log \frac{E_1}{E_2}, \quad (13)$$

where the number densities  $N_1$  and  $N_2$  are calculated for two different CR energies  $E_1$  and  $E_2$ . The electrons are injected at  $t = 0$  and are assumed not to be reaccelerated in the halo. If we neglect diffusion and assume a constant wind speed, the electrons can be considered to reside in a box while they are losing their energy due to synchrotron radiation. In this case their number density can be expressed by (Lisenfeld & Völk 2000)

$$N(E) = K_0 E^{-p} \left(1 - \frac{t}{t_{\text{syn}}}\right)^{p-1}, \quad (14)$$

where  $p$  is the injection spectral index which is assumed to be about  $p \approx 2$ . Our model describes the geometry of a “disk wind” with a vertical wind direction. Our analysis is similar to Seaquist & Odegard (1991) who made a spherical symmetric model for the wind in the central part of M 82. For the time derivative of the electron spectral index we find for  $t \rightarrow 0$

$$\frac{\Delta\gamma}{\Delta t} = (p-1) \left(\frac{1}{t_1} - \frac{1}{t_2}\right) \bigg/ \log \frac{E_2}{E_1}, \quad (15)$$

where  $t_1$  and  $t_2$  denote synchrotron lifetimes. The radio spectral index can be computed using  $\alpha = (\gamma-1)/2$ . With Eqs. (2) and (3) we can express the time derivative of the radio spectral index by

$$\frac{\Delta\alpha}{\Delta t} = \frac{B_0(\mu\text{G})^{3/2}}{\ln(\nu_1/\nu_2) \cdot 8.352 \times 10^9 \text{ yr}} \times \left( \sqrt{\frac{\nu_2}{16.1 \text{ MHz}}} - \sqrt{\frac{\nu_1}{16.1 \text{ MHz}}} \right), \quad (16)$$

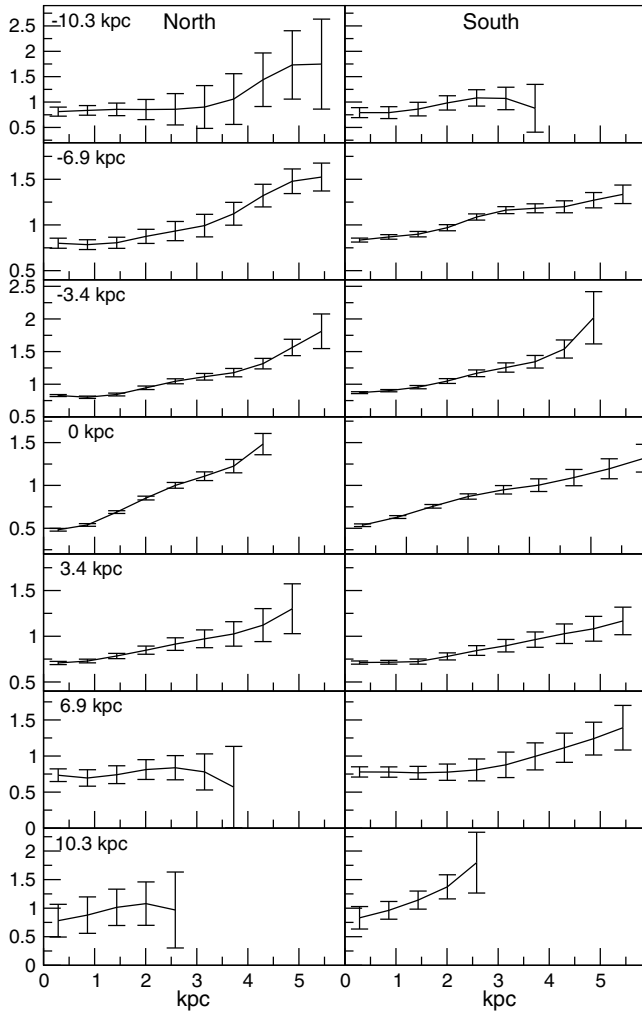


**Fig. 17.** Profiles of the spectral index between  $\lambda 90$  cm and  $\lambda 6.2$  cm perpendicular to the disk as a function of distance from the major axis. The offset of the strips along the major axis is denoted.

which only depends on the total magnetic field strength and the observation frequencies  $\nu_1$  and  $\nu_2$ . Thus, we get an expression for the average CR bulk speed  $v = \Delta z / \Delta t$

$$v = \frac{\Delta \alpha}{\Delta t} \bigg/ \frac{\Delta \alpha}{\Delta z}, \quad (17)$$

where  $\Delta \alpha / \Delta z$  is the slope of the spectral index profiles.

We applied a strip integration in order to calculate profiles of the spectral index between  $\lambda 90$  cm and  $\lambda 6.2$  cm. The strip width was  $180''$  and the pixel separation was  $15''$ . The spectral index profiles are presented in Fig. 17 where the error bars were computed from the noise in the strips, which is smaller than the noise in the map (since the width of the strips is larger than the map resolution of  $70''$ ). The spectral index distribution shows an almost linear steepening in some (but not all) of the strips. This can be explained by a constant time derivative  $\Delta \alpha / \Delta t$  and hence a constant CR bulk speed  $v$ .

The central strips at 0 kpc offset from the nucleus show a very flat spectral index for  $z < 1$  kpc. This can be explained by a thermal flattening in the nuclear region at  $\lambda 90$  cm (Carilli 1996). We restricted the analysis of the spectral index slope to heights larger than 1.4 kpc where we do not expect any contribution of the thermal gas in the disk. The resulting CR bulk speeds are

**Table 5.** Average CR bulk speeds obtained from the radio spectral index aging.

$x$	$\frac{\Delta \alpha}{\Delta z} \big _N$	$\frac{\Delta \alpha}{\Delta z} \big _S$	$B_0$	$v_N$	$v_S$
[kpc]	[kpc $^{-1}$ ]	[kpc $^{-1}$ ]	[ $\mu$ G]	[km s $^{-1}$ ]	[km s $^{-1}$ ]
-6.9	-0.22	-0.12	11	107	196
-3.4	-0.26	-0.31	14	130	109
0	-0.30	-0.26	17	150	174
3.4	-0.16	-0.12	15	234	312
6.9	-0.10	-0.20	10	204	102

shown in Table 5, where the subscripts “N” and “S” denote the northern and southern hemisphere, respectively. The mean CR bulk speed derived from the spectral index slope is  $170 \pm 70$  km s $^{-1}$ , to be compared with the CR bulk speed obtained from the scaleheights of  $v_{\lambda 6.2} = (300 \pm 30)$  km s $^{-1}$ . Since the time derivative is taken at  $t = 0$  this is a lower limit for the CR bulk speed.

## 6. Discussion

The CR distribution to constrain the transport of CRs from the disk into the halo. The local CRE lifetime is dominated by synchrotron losses and depends on the magnetic field strength in the disk which is highest in the central part. The dependence of the scaleheight on the CRE lifetime, as evident from the dumbbell shaped halo, requires a vertical CR transport.

The CR bulk speed, defined by the ratio of the CRE scaleheight to their lifetime, is constant in the northeastern halo with  $300 \pm 30$  km s $^{-1}$  and remarkably similar when applied to our observations at three different wavelengths. Thus, the local CR bulk speed is independent of the CR energy, the star-formation rate (SFR), and the magnetic field strength. Our second method to determine the CR bulk speed is to use the spectral aging of the CREs. The steepening of the observed radio spectral index with increasing distance from the galactic midplane results in a lower limit for the CR bulk speed with  $170 \pm 70$  km s $^{-1}$ . Zirakashvili & Völk (2006) made an analytical model for the CR transport in the nuclear outflow. They found by comparison with radio continuum data a velocity of 300 km s $^{-1}$  near the disk and 900 km s $^{-1}$  as terminal velocity.

Dahlem et al. (1995) and Dahlem et al. (2006) studied the CR distribution in edge-on galaxies. They found a tight and linear correlation between the radial extent of radio halos and the level of star-formation activity in the underlying disk. However, radio halos can be better studied by their vertical intensity distributions. Whereas the amplitude of the vertical profile depends on the overall radio intensity of the disk, related to the SFR, its scaleheight is determined by the outflow velocity and the CRE lifetime. The observed vertical extent also depends on the signal-to-noise ratio of the measurements. Only the scaleheight is suited to characterize the formation of radio halos.

Global radio scaleheights observed at  $\lambda 6$  cm in three edge-on galaxies with very different global SFRs were found to be similar, about 1.8 kpc for the thick radio disk (Dumke & Krause 1998; Krause 2004). This agrees well with our result of 1.7 kpc of NGC 253 which has the highest SFR of this sample. Our Eq. (9) indicates that a constant CRE scaleheight  $h_e$  in galaxies with different SFRs and hence different CRE lifetimes  $t_e$  can only be achieved if the global CR bulk speed  $v$  increases with global SFR. As all four galaxies show a dumbbell shaped radio

halo, the local scaleheight depends on the local magnetic field strength.

Since we postulate an outflow, we analyse the pressure contributions of the different ISM phases. These are the thermal gas, the kinetic energy, and the magnetic field. The thermal pressure of the halo gas is  $P_{\text{therm}} = 2n_e k_B T = 7 \times 10^{-12} \text{ erg cm}^{-3}$ , where we used an electron density of  $n_e = 8 \times 10^{-3} \text{ cm}^{-3}$  and a temperature of  $T = 3 \times 10^6 \text{ K}$  (Strickland et al. 2002). The ram pressure of the outflow is  $P_{\text{ram}} = 1/2 n_e m_p v^2 = 6 \times 10^{-12} \text{ erg cm}^{-3}$ , where  $m_p$  is the proton mass and  $v = 300 \text{ km s}^{-1}$  the wind velocity. Assuming a typical magnetic field strength of  $B = 15 \mu\text{G}$ , we find a magnetic pressure of  $P_{\text{mag}} = B^2/(8\pi) = 9 \times 10^{-12} \text{ erg cm}^{-3}$ .

If the gas in the disk were in a hydrostatic equilibrium, the gas pressure would be  $P_{\text{grav}} \approx \pi G \Sigma_g \Sigma_t$ . We obtain  $P_{\text{grav}} = 1.3 \times 10^{-11} \text{ erg cm}^{-3}$ , where we inserted  $\Sigma_g = 4 M_\odot \text{ pc}^{-2}$  for the gas surface-density (Puche et al. 1991), and  $\Sigma_m = 7.44 \times 10^{-2} \text{ g cm}^{-2}$  for the total mass surface-density (Pence 1981). We note, that the thermal pressure, the ram pressure, and the magnetic pressure are of the same order of magnitude. Since the sum of the thermal pressure, the ram pressure, and the magnetic pressure is  $2.2 \times 10^{-11} \text{ erg cm}^{-3}$ , this may indicate that the disk is not in hydrostatic equilibrium and allows outflow.

If the outflow traced by the CR transport is a galactic wind, it should finally leave the gravitational potential of the galaxy. In this case the CR bulk speed must exceed the escape velocity of  $v_{\text{esc}} = 2^{1/2} \cdot \Omega r$  (Veilleux et al. 2005), where  $\Omega r$  is the rotation velocity of the disk. Of course, the outflow may accelerate further away from the disk, below our sensitivity limit, and thus a galactic wind is possible even if the observed CR bulk speed is too low. On the other hand, a CR bulk speed above the escape velocity supports the galactic wind scenario, because it will certainly escape from the gravitational potential, unless the outflow decelerates in the halo. Using the rotation speed of  $200 \text{ km s}^{-1}$  measured by Pence (1981), we find an escape velocity of  $280 \text{ km s}^{-1}$ , which agrees within the errors with our measured CR bulk speed. Hence, a galactic wind is in NGC 253 likely and the CR transport shows the presence of a “disk wind” in the northeastern halo.

The disk wind can efficiently transport gas into the halo. The transport should be more efficient in the convective northeastern halo. Indeed, there is significantly more neutral hydrogen gas in the northeastern halo, as HI observations by Boomsma et al. (2005) show. A similar distribution is found for the ionized hydrogen, where prominent H $\alpha$  plumes are found only in the northeastern halo (Hoopes et al. 1996). This picture is corroborated by huge lobes of soft X-ray emission in the northeastern halo, which are absent in the southwestern halo (Pietsch et al. 2000). The discrepancy between the northeastern and the southwestern halo may be explained by the level of star-formation activity in the disk. Both the H $\alpha$  emission and radio continuum emission is stronger in the northeastern part of the disk. This hints to a higher SFR that can more easily drive the disk wind against the gravitational pull.

The disk wind may finally escape from the gravitational potential to the intergalactic medium (IGM). From the observations we cannot make a definite conclusion because we do not observe the transition between the radio halo and the IGM further away from the detected radio halo. With our observations we are not able to conclude whether the disk wind accelerates or decelerates within distance from the disk. With low frequency observations the scaleheight of the synchrotron emission is expected to be larger and hence the radio halo could be observed to larger vertical heights. Such data could allow us to determine whether

the disk wind accelerates as expected for a CR driven wind. Although LOFAR observations would be ideal for this purpose, the low declination of NGC 253 ( $-25^\circ$ ) requires to use the EVLA or the future SKA at frequencies as low as possible.

## 7. Conclusions

Our radio continuum study of NGC 253 shows an extended radio halo at the wavelengths from  $\lambda 90 \text{ cm}$  to  $\lambda 3.6 \text{ cm}$ . Because studies of NGC 253 need a high dynamic range, it is a difficult target for radio continuum observations. We treated the high dynamic range with a specially tailored data reduction technique. Our maps presented here are thus essentially noise limited. The combination of our new VLA mosaic map with the single-dish Effelsberg data in order to fill in the missing zero-spacing flux density allowed us to study the extra-planar continuum emission with high resolution and sensitivity. They are used to put detailed constraints on the CR transport, which lead to our main conclusions:

1. The scaleheight of the thick radio disk in the northeastern halo is a linear function of the CRE lifetime in the underlying disk at  $\lambda 90 \text{ cm}$ ,  $\lambda 20 \text{ cm}$ , and  $\lambda 6.2 \text{ cm}$ . This can be understood if the CR transport proceeds preferentially in the vertical direction.
2. The steepening of the spectral index, which is a linear function of  $z$ , can be explained by strong synchrotron losses of the CREs. The contribution of ionization losses and bremsstrahlung losses can be neglected. The adiabatic losses are of the same order of magnitude as the synchrotron losses at  $\lambda 20 \text{ cm}$  but dominate at  $\lambda 90 \text{ cm}$ .
3. We computed the CR bulk speed as the ratio of the total power scaleheight and the CRE lifetime. The CR bulk speed in the northeastern halo of  $300 \pm 30 \text{ km s}^{-1}$  is similar to the escape velocity of  $280 \text{ km s}^{-1}$ , indicating the existence of a disk wind which escapes from the gravitational potential. The local CR bulk speed is independent of the CR energy, the SFR, and the magnetic field strength.
4. The CR transport is mainly convective in the northeastern halo while in the southwestern halo the diffusion of CRs is significant. We measure an average diffusion coefficient of  $2.0 \pm 0.3 \times 10^{29} \text{ cm}^2 \text{ s}^{-1}$ .
5. The disk wind is the driving source for the luminous gas in the halo. In the convective northeastern halo the gas is transported more efficiently from the disk into the halo than in the diffusive southwestern halo. This can explain the different amounts of extra-planar gas in these two halo parts as observed in HI, H $\alpha$ , and soft X-rays.

The CR transport is always the superposition of convection and diffusion. The data presented here provide a basis for more detailed calculations using the combined diffusion and convection equation. These calculations should include vertical profiles of the magnetic field strength, the CR number density, and the velocity of the galactic wind.

*Acknowledgements.* We appreciate the comments of our referee, Timothy Paglione, which improved the paper significantly. We thank Michael Dumke and the Effelsberg staff for help with the observations. It is our pleasure to thank Reinhard Schlickeiser and Dieter Breitschwerdt for inspiring discussions. We are grateful to Enno Middelberg and Wolfgang Reich for valuable comments on the manuscript.

V.H. would like to thank the organizers of the Graduiertenkolleg GRK 787 and the Sonderforschungsbereich SFB 591 for support and funding during the course

of his PhD. The GRK 787 ‘‘Galaxy groups as laboratories for baryonic and dark matter’’ and the SFB 591 ‘‘Universal properties of non-equilibrium plasmas’’ were funded by the Deutsche Forschungsgemeinschaft (DFG).

## Appendix A: The synchrotron lifetime within an exponential magnetic field profile

In order to calculate the CR bulk speed in Sect. 5.4 we used the synchrotron lifetime of the electrons. Since we do not know the vertical distribution of the magnetic field, we assumed a constant magnetic field strength. In reality, however, we expect the magnetic field strength to have a vertical, decreasing profile. In this section we investigate the difference between the synchrotron lifetime for a constant magnetic field and for an exponential vertical profile.

The exponential profile of the magnetic field reads

$$B(z) = B_0 \exp(-z/h_B), \quad (\text{A.1})$$

where  $B_0$  is the maximum magnetic field strength and  $h_B$  the scaleheight of the magnetic field. Replacing  $t = z/v$ , where we assume a constant CR bulk speed, the differential of the energy is:

$$dE = -\frac{\sigma_T c B(z)^2}{8\pi} \left( \frac{E(z)}{mc^2} \right)^2 \frac{dz}{v}. \quad (\text{A.2})$$

We integrate this differential equation by separating the variables with:

$$\frac{dE}{E^2} = -\frac{\sigma_T B(z)^2}{8\pi m^2 c^3 v} dz. \quad (\text{A.3})$$

Now we integrate from  $z = 0$  to  $z$ :

$$\int_{E_0}^E \frac{dE}{E^2} = \int_{z=0}^z -\frac{\sigma_T B_0^2}{8\pi m^2 c^3 v} \exp(-2z/h_B) dz, \quad (\text{A.4})$$

where we inserted the exponential profile of  $B$ . Finally, we find for the vertical CRE energy profile

$$E(z) = \frac{E_0}{1 + \frac{E_0 h_B \sigma_T B_0^2}{16\pi m^2 c^3 v} \cdot (1 - \exp(-2z/h_B))}. \quad (\text{A.5})$$

If we use the definition for the synchrotron lifetime for a constant field strength  $B_0$

$$t_{\text{syn},0} = \frac{8\pi m^2 c^3}{E_0 B_0^2} \quad (\text{A.6})$$

we find

$$E_B(z) = \frac{E_0}{1 + \frac{h_B}{2t_{\text{syn},0}v} \cdot (1 - \exp(-2z/h_B))}. \quad (\text{A.7})$$

For the case of a constant magnetic field strength we have as energy profile:

$$E_{B0}(z) = \frac{E_0}{1 + \frac{z}{t_{\text{syn},0}v}}. \quad (\text{A.8})$$

Clearly, the larger the scaleheight of the magnetic field, the smaller is the difference between the two CRE energy profiles. We now use  $h_B = 4 \cdot h_{\text{syn}}$  as a lower limit due to the equipartition condition (see Eq. (1)), where we set  $\alpha_{\text{nt}} = 1$ . In Fig. A.1 we

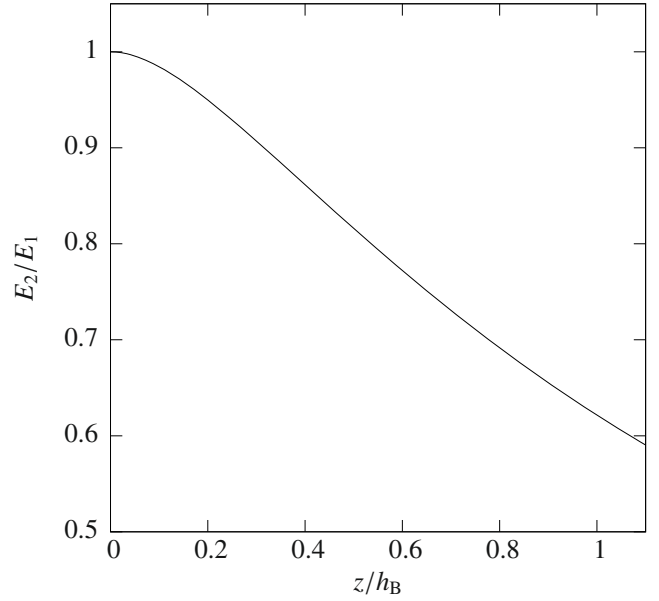


**Fig. A.1.** Ratio of the two energies  $E_{B0}/E_B$  as a function of  $z$ . For  $E_B$  the magnetic field has an exponential distribution with a scaleheight  $h_B$  while for  $E_{B0}$  it is constant.

plot the ratio of the energies  $E_{B0}/E_B$  as a function of  $z$  in units of  $h_B$ . Any estimate of the error made using a constant magnetic field instead of an exponential magnetic field must be averaged using the weight of the points. If we restrict  $z < h_{\text{syn}}$  and take into account that the inner points have larger weights (due to the higher synchrotron emission), the error estimate is around 10%. Hence, in our case the assumption of a constant magnetic field strength for the calculation of the CRE energy and hence of the synchrotron lifetime in Sect. 5.3 is acceptable.

## References

- Baars, J. W. M., Genzel, R., Pauliny-Toth, I. I. K., & Witzel, A. 1977, *A&A*, 61, 99
- Beck, R., & Krause, M. 2005, *AN*, 326, 414
- Beck, R., Biermann, P., Emerson, D. T., & Wielebinski, R. 1979, *A&A*, 77, 25
- Beck, R., Carilli, C. L., Holdaway, M. A., & Klein, U. 1994, *A&A*, 292, 409
- Beck, R., Brandenburg, A., Moss, D., Shukurov, A., & Sokoloff, D. 1996, *ARA&A*, 34, 155
- Boomsma, R., Oosterloo, T., Fraternali, F., van der Hulst, J. M., & Sancisi, R. 2005, *A&A*, 431, 65
- Braun, R. 1988, *Millimeter Array Memo*, 46
- Breitschwerdt, D., McKenzie, J. F., & Voelk, H. J. 1991, *A&A*, 245, 79
- Breitschwerdt, D., McKenzie, J. F., & Voelk, H. J. 1993, *A&A*, 269, 54
- Carilli, C. L. 1996, *A&A*, 305, 402
- Carilli, C. L., Holdaway, M. A., Ho, P. T. P., & de Pree, C. G. 1992, *ApJ*, 399, L59
- Dahlem, M., Lisenfeld, U., & Golla, G. 1995, *ApJ*, 444, 119
- Dahlem, M., Lisenfeld, U., & Rossa, J. 2006, *A&A*, 457, 121
- Dumke, M., & Krause, M. 1998, in *The Local Bubble and Beyond*, ed. D. Breitschwerdt, M. J. Freyberg, & J. Truemper (Berlin: Springer Verlag), IAU Colloq., 166, Lect. Notes Phys., 506, 555
- Dumke, M., Krause, M., Wielebinski, R., & Klein, U. 1995, *A&A*, 302, 691
- Emerson, D. T., & Gräve, R. 1988, *A&A*, 190, 353
- Emerson, D. T., Klein, U., & Haslam, C. G. T. 1979, *A&A*, 76, 92

- Everett, J. E., Zweibel, E. G., Benjamin, R. A., et al. 2008, *ApJ*, 674, 258
- Field, G. B., Goldsmith, D. W., & Habing, H. J. 1969, *ApJ*, 155, 149
- Green, D. A. 2002, in *The Universe at Low Radio Frequencies*, ed. A. Pramesh Rao, G. Swarup, & Gopal-Krishna, IAU Symp., 199, 276
- Haslam, C. G. T. 1974, *A&AS*, 15, 333
- Heckman, T. M., Lehnert, M. D., Strickland, D. K., & Armus, L. 2000, *ApJS*, 129, 493
- Heesen, V. 2008, Ph.D. Thesis, Ruhr-Universität, Bochum, Germany
- Högbom, J. A. 1974, *A&AS*, 15, 417
- Hoopes, C. G., Walterbos, R. A. M., & Greenwalt, B. E. 1996, *AJ*, 112, 1429
- Ipavich, F. M. 1975, *ApJ*, 196, 107
- Karachentsev, I. D., Grebel, E. K., Sharina, M. E., et al. 2003, *A&A*, 404, 93
- Klein, U., & Mack, K.-H. 1995, in *Multi-Feed Systems for Radio Telescopes*, ed. D. T. Emerson, & J. M. Payne, ASP Conf. Ser., 75, 318
- Krause, M. 2004, in *The Magnetized Interstellar Medium*, ed. B. Uyaniker, W. Reich, & R. Wielebinski, 173
- Lehnert, M. D., & Heckman, T. M. 1996, *ApJ*, 472, 546
- Lisenfeld, U., & Völk, H. J. 2000, *A&A*, 354, 423
- Morsi, H. W., & Reich, W. 1986, *A&A*, 163, 313
- Niklas, S., Klein, U., & Wielebinski, R. 1997, *A&A*, 322, 19
- Pence, W. D. 1980, *ApJ*, 239, 54
- Pence, W. D. 1981, *ApJ*, 247, 473
- Pietsch, W., Vogler, A., Klein, U., & Zinnecker, H. 2000, *A&A*, 360, 24
- Pohl, M. 1990, Diploma thesis, Max-Planck-Institut für Radioastronomie, Bonn, Germany
- Pohl, M., & Schlickeiser, R. 1990, *A&A*, 239, 424
- Ptuskin, V. S., Voelk, H. J., Zirakashvili, V. N., & Breitschwerdt, D. 1997, *A&A*, 321, 434
- Puche, D., Carignan, C., & van Gorkom, J. H. 1991, *AJ*, 101, 456
- Radovich, M., Kahanpää, J., & Lemke, D. 2001, *A&A*, 377, 73
- Rottmann, H. 1996, Ph.D. Thesis, Friedrichs-Wilhelms-Universität, Bonn, Germany
- Rybicki, G. B., & Lightman, A. P. 1986, *Radiative Processes in Astrophysics* (Wiley-VCH)
- Schulz, H., & Wegner, G. 1992, *A&A*, 266, 167
- Seaquist, E. R., & Odegard, N. 1991, *ApJ*, 369, 320
- Strickland, D. K., Heckman, T. M., Weaver, K. A., & Dahlem, M. 2000, *AJ*, 120, 2965
- Strickland, D. K., Heckman, T. M., Weaver, K. A., Hoopes, C. G., & Dahlem, M. 2002, *ApJ*, 568, 689
- Suchkov, A. A., Balsara, D. S., Heckman, T. M., & Leitherner, C. 1994, *ApJ*, 430, 511
- Thompson, T. A., Quataert, E., Waxman, E., Murray, N., & Martin, C. L. 2006, *ApJ*, 645, 186
- Veilleux, S., Cecil, G., & Bland-Hawthorn, J. 2005, *ARA&A*, 43, 769
- Zirakashvili, V. N., & Völk, H. J. 2006, *ApJ*, 636, 140
- Zirakashvili, V. N., Breitschwerdt, D., Ptuskin, V. S., & Voelk, H. J. 1996, *A&A*, 311, 113